Article

Mapping charge excitations in generalized Wigner crystals

In the format provided by the
authors and unedited

Table of Contents

1. Normalization of the dI/dV spectra

To make charging peaks features in the dI/dV spectra more visible, we reduce the background signal through a special normalization process. Here we take Fig. 2a and 2b in the main text as an example to illustrate this process. We first note that the strong background signal is mainly determined by the graphene density of states, which do not significantly change with the tuning of the backgate voltage V_{BG}. On the other hand, the tip-induced charging peaks have a strong dependence on V_{BG} (see detailed explanation in the main text), and show a very dispersive feature in the 2D plot of the V_{BG}-dependent dI/dV spectra. To obtain the V_{BG}-independent background signal we average all the dI/dV spectra (which average out the fast-changing charging peaks) (blue curve in Fig. S1b). Dividing the raw dI/dV spectra (several typical raw dI/dV spectra are shown in Fig. S1b as red curves) by this averaged dI/dV spectra allows us to obtain the normalized dI/dV spectra. Several typical normalized dI/dV spectra are shown in Fig. S1c. The complete data set of the normalized dI/dV spectra is shown in the 2D color plot in Fig. S1d (same as Fig. 2b in the main text).

The same normalization process is applied to the high-resolution V_{BG}-dependent dI/dV spectra measured around the n = 2/3 state shown in Fig. 2c in the main text (with the raw data shown in Fig. S1e). Several typical raw dI/dV spectra and the corresponding normalized spectra are shown in Fig. S1f and S1g, respectively. The complete data set of the normalized dI/dV spectra are shown in Fig. 2c in the main text (also reproduced in Fig. S1h).
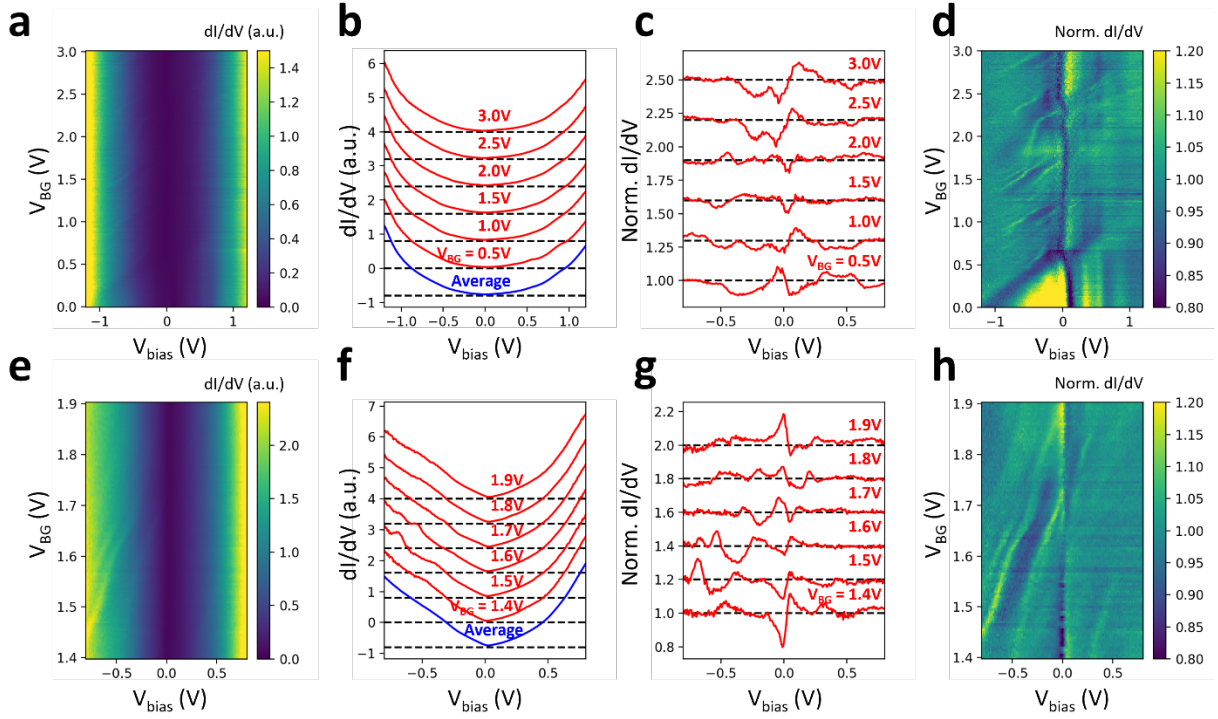
Figure S1. Normalization of the V_{BG}-dependent dI/dV spectra. a. 2D plot of the raw data for the V_{BG}-dependent dI/dV spectra, same as Fig. 2a in the main text. **b**. The red curves show typical dI/dV spectra measured at different V_{BG}, while the blue curve shows the mean dI/dV spectra averaged over all spectra shown in **a**. **c**. Normalized dI/dV spectra obtained by dividing the raw spectra (red curves) by the averaged spectra (blue curves) shown in **b**. **d**. 2D plot of the normalized data shown in **a**, same as Fig. 2b in the main text. **e**. 2D plot of the raw data for the dI/dV spectra shown in Fig. 2c of the main text. **f**. The red curves show several typical dI/dV spectra measured at different V_{BG}, while the blue curve shows the mean dI/dV spectra averaged over all spectra shown in **e**. **g**. Normalized dI/dV spectra obtained by dividing the raw spectra (red curves) by the average spectra (blue curve) shown in **f**. **g**. 2D plot of the normalized data shown in **e**, same as Fig. 2c in the main text. **h**. 2D plot of the normalized data shown in **e**.

Spectra in **b**, **c**, **f**, and **g** are shifted vertically for clarity, with the corresponding zero reference point labeled by black dashed lines.

2.   Origin of the charging dI/dV peak

We first note that the tip-induced charging peak assisted by the long-range tip-sample Coulomb interactions has been studied in several different material systems where the general mechanism has been described[1-5]. Below, we focus on its application in our SSEC spectroscopy.

Fig. S2a reproduces the charging peak phase diagram in Fig. 2e of the manuscript. Due to the tip-graphene work function difference (Pt/Ir tip :5.0eV to 5.9eV, top graphene: ~4.5eV), a negative bias voltage V_{bias0} is required to compensate the work function difference so that a zero electrical field is between the tip and the charge neutral graphene. The charging (electron injection) and discharging (hole injection) events take place at a bias voltage V_{bias} lower and higher than V_{bias0}, respectively.

Let's consider three representative charging transition regions denoted by the green arrows and labeled as A, B, and C in Figure S2a: A. Electron excitation with $V_{bias} < V_{bias0} < 0$; B. Hole excitation with $V_{bias0} < V_{bias} < 0$; and C. Hole excitation with $V_{bias} > 0$. The graphene layer is close to the charge neutral point. In region A, the excitation of an electron quasiparticle in the TMD layer with an increased negative V_{bias} makes the top monolayer graphene more hole doped locally due to the Coulomb interaction between the TMD and graphene layers. It lowers the local graphene Fermi level (Fig. S2b) that increases the number of available tunneling channels (labeled in blue). Consequently, it increases the absolute tunneling current (i.e., the current becomes more negative, right pannel of Fig. S2b), yielding a dI/dV peak. In region B, the excitation of a hole quasiparticle in the TMD with a decreased negative V_{bias} lifts the monolayer graphene Fermi level (Fig. S2c), that decreases the number of available tunneling channels and hence decreases the absolute tunneling current (less negative, right pannel of Fig. S2c). In region C, the excitation of a hole in

the TMD layer with an increased positive V_{bias} similarly lifts the top graphene Fermi level, but it increases the number of available tunneling channels (due to the reversed V_{bias} polarity, Fig. S2d) and hence increase the absolute tunneling current (more positive current, right pannel of Fig. S2d).

Based on the above analysis, there is always a jump of tunneling current whenever an electron or hole charging event takes place due to the resulting change in the local graphene doping. They all lead to a dI/dV peak on the top graphene sensing layer, as observed in our experiment.
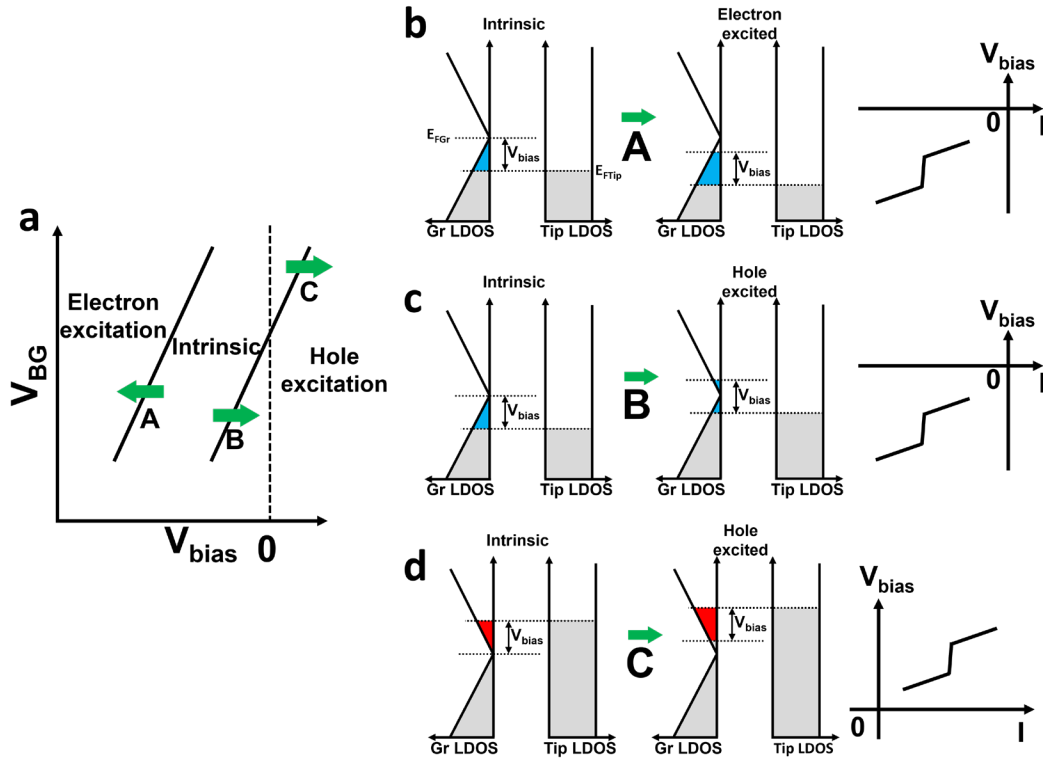

Figure S2. Illustration for the origin of the dI/dV charging peaks. a. the charging peak phase diagram reproduced from Fig. 2e of the manuscript. Three representative charging transition regions are considered here: A. Electron excitation with $V_{bias} < 0$, B. Hole excitation with $V_{bias} < 0$, and C. Hole excitation with $V_{bias} > 0$ (labeled with green arrows). **b**. Tunneling energy diagram before and after excitation A. The graphene layer is close to the charge neutral point. An electron

6

excitation in TMD driven by an increased negative V_{bias} makes the top graphene more hole-doped and lowers its Fermi level E_{FGr}. It increases the number of available tunneling channels (labeled in blue) and hence the tunneling current (right pannel). **c**. Tunneling energy diagram before and after excitation B. A hole excitation in the TMD layer driven by a decreased negative V_{bias} makes the graphene more electron doped. It decreases the available tunneling channels and hence the tunneling current (right pannel). **d**. Tunneling energy diagram before and after excitation C. A hole excitation in the TMD layer driven by an increased positive V_{bias} similarly makes the graphene more electron doped. However, it increases the available tunneling channels (labeled in red) due to the reversed V_{bias} polarity and hence enlarges the tunneling current (right pannel).

3. Determination of the filling factors via dI/dV mapping

The filling factor of the moire superlattice is not only determined by the simple capacitor model, but also directly through dI/dV mapping of the electron lattice. For example, the filling factor of the n=2/3 state can be determined through the mapping shown in Fig. 3 in the main text. Several typical results are shown in Fig. S3, including mapping for addition of electrons to the n = 0 state (Fig. S3a and S3b) and addition of holes in the n = 1 state (Fig. S3c and S3d).
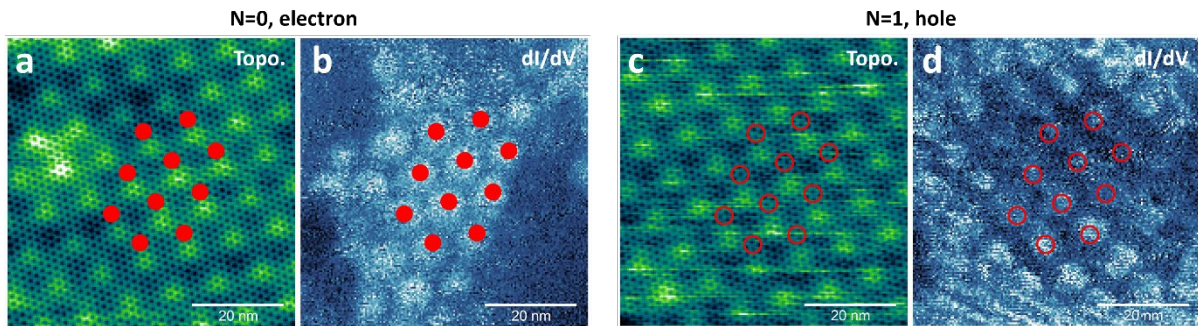

Figure S3. Determination of the filling factor. a. Typical STM topography of sensing layer. Red dots denote electron excitation locations. **b**. dI/dV mapping of the electron quasiparticle in the n = 0 state measured in the same area as in **a** (V_{bias} = -0.75V, V_{BG} = 0.43V, V_{TG} = 0.52V). The position of the electrons is labeled with red solid dots **c**. Typical STM topography of sensing layer. Red circles denote hole excitation locations. **d**. dI/dV mapping of the hole quasiparticle in the n =1 state measured in the same area as in **c** (V_{bias} = 0.20V, V_{BG} = 2.4V, V_{TG} = 0.52V). The positions of the holes are labeled with red circles.

4. Electrostatic simulation of the correlation between α and α/β

In this section, we introduce details for the electrostatic simulation of correlation between α and α/β, where α and β are the tip-t-WS$_2$ and backgate-t-WS$_2$ coupling constants, respectively. Particularly, the graphene quantum capacitance effect is included in the simulation. The backgate graphite is modeled by an infinitely large metallic plate. Due to the unknown geometry of the STM tip, we model the tip in two extreme situations: (1) as a metallic cone (illustrated in Fig. S4a) and (2) as a metallic sphere (illustrated in Fig. S4d). In the conic tip model, the tip geometry is controlled by the half cone angle θ and tip height h (separation between tip apex and the graphene surface), while the spherical tip model, the tip geometry is controlled by the sphere radius and tip height (separation between sphere bottom and the graphene surface). The t-WS$_2$ moire heterostructure is regarded as a thin insulator since it is in a correlated insulating state. The t-WS$_2$ is incorporated into the surrounding hBN and regarded as an insulator with the same dielectric constant as the hBN. The graphene is modeled by a special boundary condition whose electrical potential V_{Gr} is related to its charge density ρ_{Gr} due to the graphene quantum capacitance: $V_{Gr} = V_{Gr}(\rho_{Gr})$, as described below.

The graphene surface electrical potential $V_{Gr}(\rho_{Gr})$, namely its vacuum level, can be determined in the following way. Since the graphene is connected to a voltage source, meaning its chemical potential is fixed externally, then the change of the graphene surface electrical potential $\Delta V_{Gr} = V_{Gr} - V_{Gr0}$ can be determined as $\Delta V_{Gr} = \Delta E_f/e$, where $\Delta E_f = E_f - E_{f0}$ is the graphene Fermi level change. Here V_{Gr0} and E_{f0} are the graphene surface electrical potential and Fermi level at charge neutrality ($\rho_{Gr} = 0$). For simplicity, we assume $V_{Gr0} = 0$ and $E_{f0} = 0$. Therefore, we

have $V_{Gr} = E_f/e$. The relation between the graphene Fermi level E_f and its carrier density n_{Gr} is determined by

$$n_{Gr} = \begin{cases} \int_0^{E_f} DOS_{Gr}(E)dE, & (E_f \geq 0) \\ \int_{E_f}^0 DOS_{Gr}(E)dE, & (E_f < 0) \end{cases},$$

where $DOS_{Gr}(E) = \frac{2}{\pi} \cdot \frac{|E|}{(\hbar v_F)^2}$ is the graphene density of states per unit area. Here $v_F = 10^6 m/s$ is the Femi velocity of the graphene. Using $\rho_{Gr} = -en_{Gr}$, we obtain the following boundary condition for the graphene plane

$$V_{Gr}(\rho_{Gr}) = \begin{cases} \frac{\sqrt{\pi}\hbar v_F}{e} \cdot \sqrt{-\frac{\rho_{Gr}}{e}}, & (\rho_{Gr} < 0) \\ -\frac{\sqrt{\pi}\hbar v_F}{e} \cdot \sqrt{\frac{\rho_{Gr}}{e}}, & (\rho_{Gr} \geq 0) \end{cases},$$

This boundary condition reflects the quantum capacitance of the graphene and its partial screening effect.

In the simulation, the boundary conditions for the tip and backgate are set at $V = V_{bias}$ and $V = V_{BG}$, respectively. To make the simulation more computable we have a cylindrically truncated grounded surface enclose the simulation center. The dielectric constants in the region above and below the graphene are set to $\varepsilon_{vac} = \varepsilon_0$ and $\varepsilon_{hBN} = 4.2\varepsilon_0$, respectively, where ε_0 is the vacuum dielectric constant. α and β are obtained via monitoring the responses of the electrical potential change $\Delta\Phi$ at the position of the charged site ($r = 5.4nm$ when the tip is fixed at the three-site symmetric point) in the TMD layer with the following parameters: α: $V_{bias} = 145mV$ and $V_{BG} = 0$, and β: $V_{bias} = 0$ and $V_{BG} = 71$ mV.

Fig. S4b and S4c show two typical simulated electrical potential distribution for the conic tip model with either only nonzero V_{BG} applied (Fig. S4b, $V_{bias} = 0$ and $V_{BG} = 71$ mV) or only nonzero V_{bias} applied (Fig. S4c, $V_{bias} = 145$mV and $V_{BG} = 0$). The simulation parameters used here are $\theta = 54.95°$ and $h = 1nm$. Fig. S4e and S4f show two typical simulated electrical potential distribution for the spherical tip model with either only V_{BG} applied (Fig. S4e, $V_{bias} = 0$ and $V_{BG} = 71$ mV) or only V_{bias} applied (Fig. S4f, $V_{bias} = 145$mV and $V_{BG} = 0$). The simulation parameters used here are $R = 14nm$ and $h = 2.06nm$.

Next, we investigate the tip geometry dependence of α and β. For clarity, we use the subscript "cone" and "sphere" to distinguish the two different models. For the conic model, Fig. S5a and S5b shows the simulated for α_{cone} (Fig. S5a) and β_{cone} (S5b) as functions of θ and h. Particularly, θ ranges from 15° to 85°, and h ranges from 0.1nm to 9nm. Such a range should be large enough to cover the situation of realistic STM tips. The change of the tip geometry significantly affects individual coupling constants, where α_{cone} is affected more while β_{cone} is affected less. To compare with the experimentally determined α/β ratio (reflected by the charging peak slopes in Fig. 2b and 2c of the manuscript), Fig. S5c displays the simulated $\alpha_{cone}/\beta_{cone}$ as functions of θ and h. We can similarly investigate the geometry dependence of the spherical model. Fig. S5d and S5e show the simulated for α_{sphere} (Fig. S5d) and β_{sphere} (S5e) as functions of R and h. Fig. S5f show the simulated ratio $\alpha_{sphere}/\beta_{sphere}$ as functions of R and h.

Now we can examine the correlation of the coupling constant α (to de determined) and the ratio α/β (experimentally measurable) for different tip geometries (varying tip height, cone angle, sphere radius). Fig. S6a shows the scatter plot of the α value from Fig. S5a and S5d versus the α/β value from Fig. S5c and S5f for all studied tip geometries. The conic and spherical results are

plotted with blue and orange points, respectively. It can be seen that α and α/β exhibit an almost

one-to-one monotonic correspondence that is largely independent of the detailed tip geometry. Fig.

S6b shows a zoom-in scatter plot of α versus α/β corresponding to the dashed box region in Fig.

S6a, further confirming the well-defined one-to-one correspondence between α and α/β

independent of the tip geometry. Such a geometry-independent correspondence naturally defines

a calibration relation enabling to reliably determine the coupling constant $\alpha = 0.16$ based on the

experimentally determined $\alpha/\beta = 0.51$. The uncertainty of the obtained α due to the unknow tip

geometry (such as the vastly different cone and sphere) is less than 3%. We note that this simulated

coupling constant is close to values reported in previous work[6].

Finally, we note that the potential response of the charged site $\Delta\Phi$ is not strictly linear with

the change of V_{bias} and V_{BG}. This is shown in Fig. S7a ($\Delta\Phi$ as a function of V_{bias}) and S7b ($\Delta\Phi$ as

a function of V_{BG}). This effect occurs because at large tip bias or backgate voltage the graphene is

strongly doped and has a larger density of states at the Fermi level and behaves more like a metal.

However, in the measurement range $V_{bias} < 200mV$ and $V_{BG} < 100mV$ the response can still be
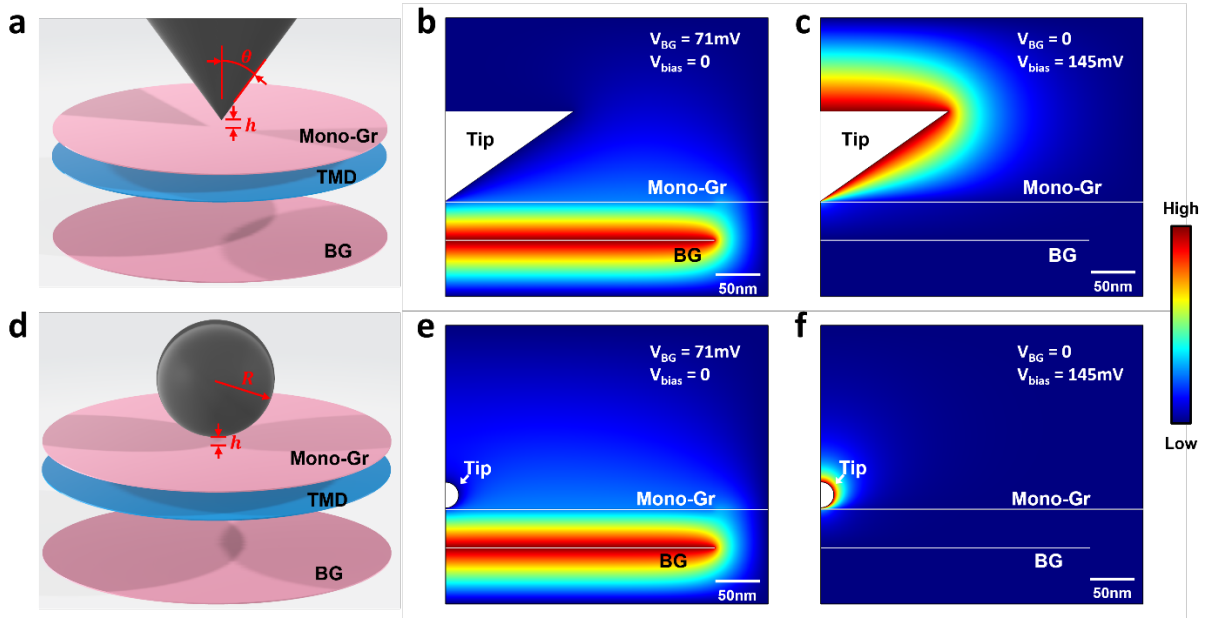
approximately regarded as being linear.

Figure S4. Electrostatic simulation of the SSEC spectroscopy. a. Schematic of the conic tip model. The tip is represented by an ideal metallic cone with half cone angle θ and tip height h (separation between tip apex and the graphene surface). The backgate is modeled by an ideal metallic plate. The graphene is modeled as follows: we set the boundary conditions on the graphene surface to be that the electrical potential is determined by the charge density so that the quantum capacitance of the graphene can be correctly treated. See more details in section 3. **b-c.** Simulated electrical potential distribution for the conic tip model with (**b**) $V_{BG} = 71$mV and $V_{bias} = 0$, and (**c**) $V_{BG} = 0$ and $V_{bias} = 145$mV. The simulation parameters used are $\theta = 54.95°$ and $h = 1nm$. The position of the t-WS$_2$ layer is not depicted here since it is regarded as an insulator with a dielectric constant equivalent to that of hBN. **d.** Schematic of the spherical tip model. The configuration is mostly the same as the one in (**a**) expect that the tip is modeled as an ideal metallic sphere with radius R here. **e-f.** Simulated electrical potential distribution for the spherical tip model with (**b**) $V_{BG} = 71$mV and $V_{bias} = 0$, and (**c**) $V_{BG} = 0$ and $V_{bias} = 145$mV. The simulation parameters used are $R = 14nm$ and $h = 2.06nm$.
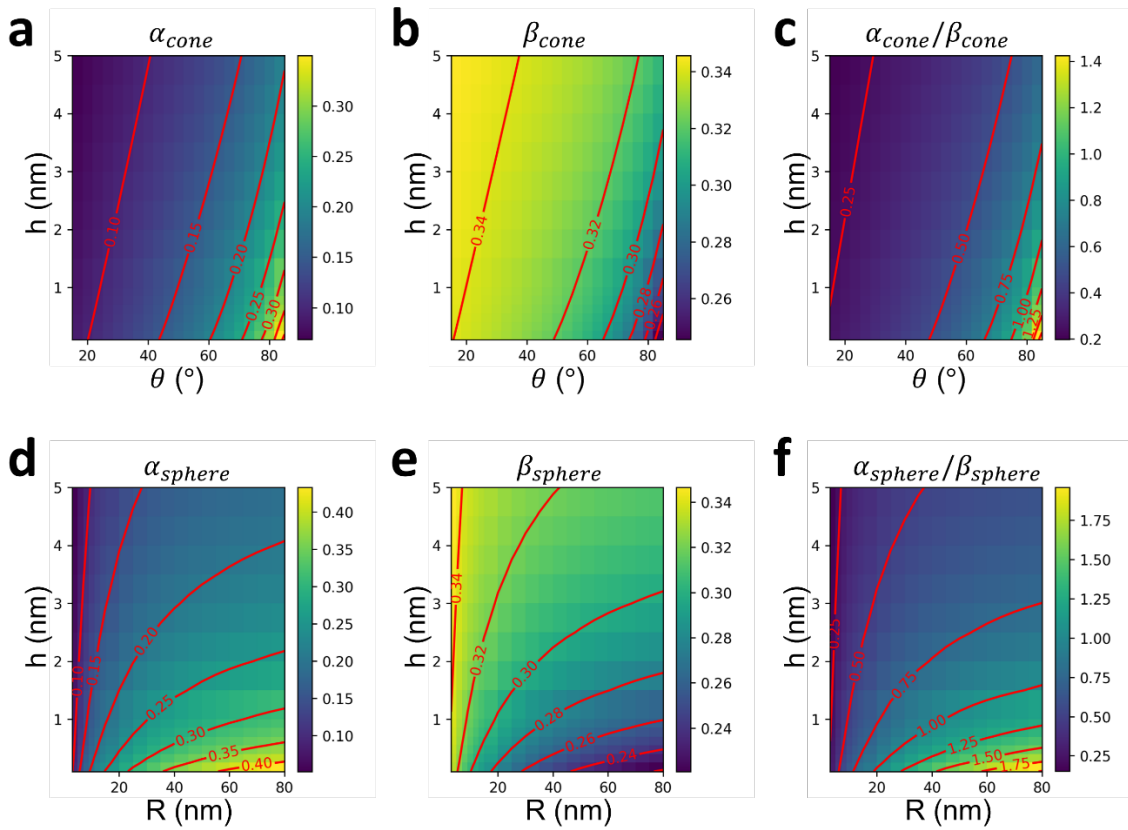
Figure S5. Simulated results for the tip-TMD coupling constant. a-c. Simulated results for the conic tip model: (**a**) α_{cone}, (**b**) β_{cone}, and (**c**) $\alpha_{cone}/\beta_{cone}$ as functions of the tip height h and the cone angle θ. Contour lines are labeled in red in (**a-c**) for clarity. **a-c.** Simulated results for the conic tip model: (**a**) α_{cone}, (**b**) β_{cone}, and (**c**) $\alpha_{cone}/\beta_{cone}$ as functions of the tip height h and the cone angle θ. **d-f.** Simulated results for the conic tip model: (**d**) α_{sphere}, (**e**) β_{sphere}, and (**f**) $\alpha_{sphere}/\beta_{sphere}$ as functions of the tip height h and the cone angle θ. Contour lines are labeled in red in (**a-f**) for clarity.
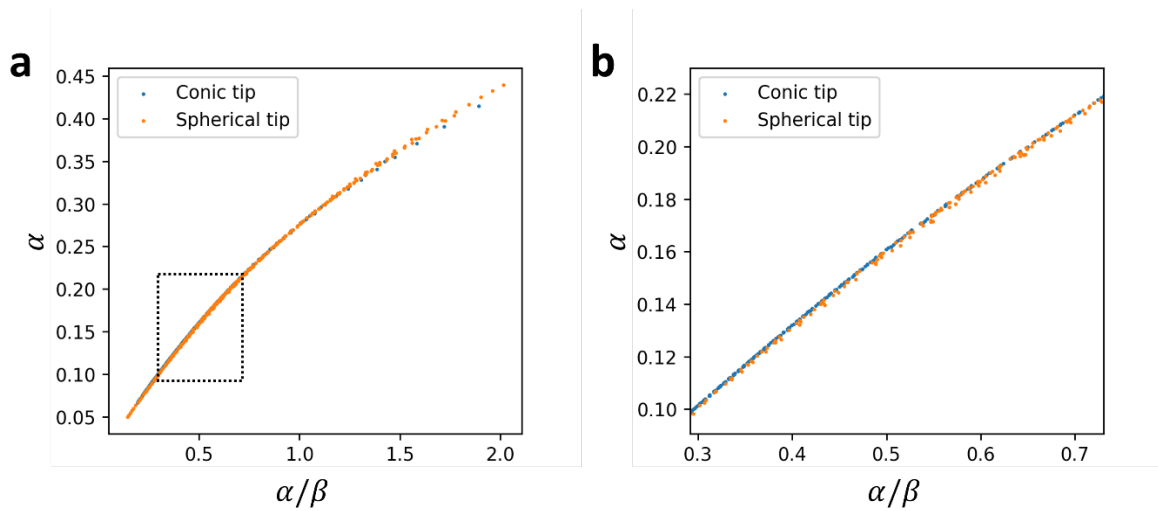
Figure S6. Simulated results for α as a function of α/β. a. Scatter plot of the α data in Fig. R5a and R5d versus the α/β data in Fig. R5c and R5f. Results for the conic and spherical models are plotted with blue and orange points, respectively. **b**. Zoom-in scatter plot of α versus α/β corresponding to the dashed box region in (**a**). α and α/β exhibit well-defined one-to-one monotonic correspondence that is nearly independent of the specific tip geometry parameters (h and θ (or R)). Such a correspondence naturally defines a calibration relation that enable us to obtain the tip-TMD coupling constant $\alpha = 0.16$ from the experimentally determined ratio $\frac{\alpha}{\beta} = 0.51$.
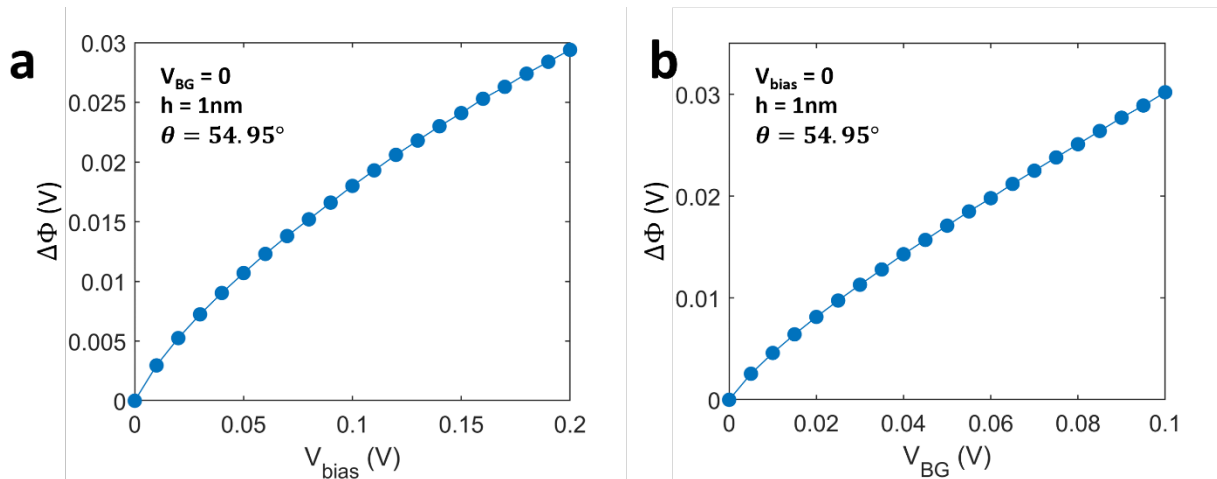
Figure S7 Potential change ΔΦ as functions of V$_{bias}$ and V$_{BG}$ for the conic tip model. a. ΔΦ at r=5.4nm in the TMD layer for different V$_{bias}$ values at V$_{BG}$ = 0. **b**. Potential change ΔΦ at r=5.4nm in the TMD layer for different V$_{BG}$ values at V$_{bias}$ = 0. h = 1nm and $\theta = 54.95°$ used for simulating the conic tip model here.

5. V_{TG} dependence of the dI/dV spectra

Fig. S8 shows the normalized dI/dV spectra around the n = 2/3 state measured at the $B^{S/S}$ site with V_{TG} = 0.52V (Fig. S8a) and 0.49V (Fig. S8b). We note that even a small change of V_{TG} can significantly change the relative doping in the graphene and the TMD layer (due to the very thin hBN in between) and modify the discharging behavior. As shown in Fig. S8, decreasing V_{TG} from 0.52V (Fig. S8a) to 0.49V (Fig. S8b) shifts the hole charging peak branch to a more positive V_{bias} and a much larger V_{BG}. As shown in Fig. S8b, the hole charging branch is prominent over a large V_{bias} range at V_{TG} = 0.49V, which extends to the V_{bias} > 0 region. In contrast, Fig. S8a shows that the hole charging branch has a narrower range for V_{TG} = 0.52V. Therefore, we chose V_{TG} = 0.49V to best show the hole charging ring evolution behavior in Fig. 3h-k of the main text.
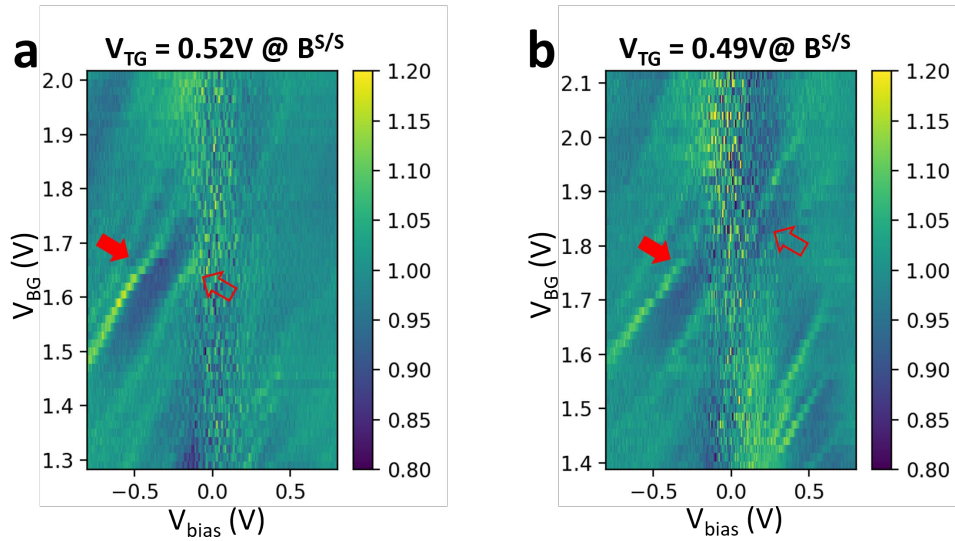

Figure S8. V_{TG}-dependent normalized dI/dV spectra for the n = 2/3 state. a. V_{TG} = 0.52V, **b**. V_{TG} =0.49V. Both are measured at the $B^{S/S}$ site around the n = 2/3 state with the same tip status. Red solid arrows label the electron charging branch while red hollow arrow labels the hole charging branch.

6. Stacking site dependence of the dI/dV spectra

Fig. S9 shows the normalized dI/dV spectra measured at the $B^{S/S}$ site (Fig. S9a, reproduced from Fig. 2b of the main text), the electron filled $B^{W/W}$ site (Fig. S9b), and the electron empty $B^{W/W}$ site (Fig. S9c) for the n = 2/3 generalized Wigner crystal state under the same tip status. Compared with the $B^{S/S}$ site (Fig. S9a), the electron filled $B^{W/W}$ site (Fig. S9b) features a stronger and more dispersive hole charging peak (top right) and a weaker and less dispersive electron charging peak (bottom left). The electron empty $B^{W/W}$ site (Fig. S9c) shows an opposite feature: stronger and more dispersive electron charging peak (bottom left) and weaker and less dispersive hole charging peak (top right). The red dots and circles in Fig. 2c of the main text are also labeled in Fig. S9a-c at the same position for reference.
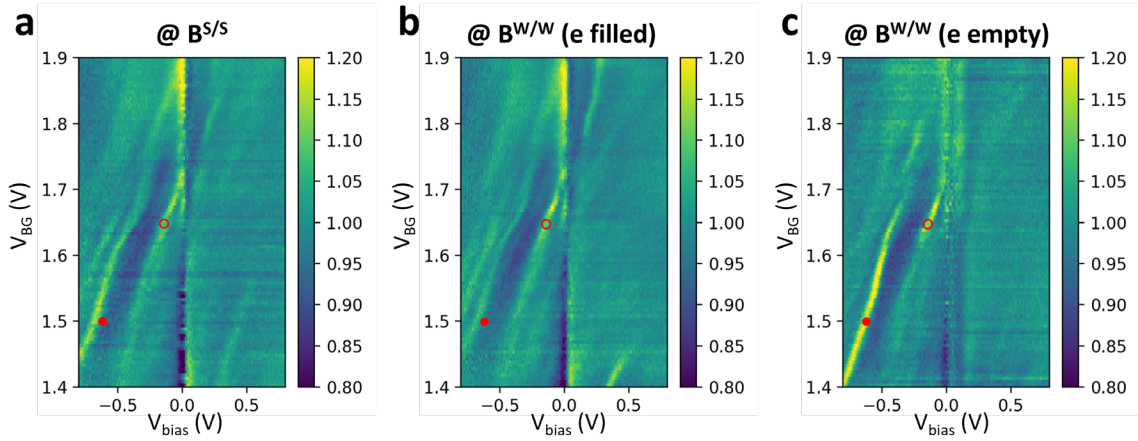

Figure S9. Site-dependent normalized dI/dV spectra for the n = 2/3 state. a. $B^{S/S}$ site, reproduced from Fig. 2b of the main text. **b**. electron filled $B^{W/W}$ site. **c**. electron empty $B^{W/W}$ site. V_{TG} is fixed at 0.52V. The red dots correspond to V_{BG} = 1.50V and V_{bias} = -0.59V while the red circles correspond to V_{BG} = 1.65V and V_{bias} = -0.14V.

7. Determination of ΔV_{bias} for the gaps of the correlated states

We note that in Fig. 2b and c, there exists a fluctuation of ΔV_{bias}. To obtain the values of ΔV_{bias} in a more precise and statistical way, we performed line fitting of the dispersive electron and hole charging peaks and extract the value of ΔV_{bias} by evaluating the horizontal gap between the fitted lines. The details of this fitting procedure are described below.

We first identify the peak positions of the closest pair of electron and hole charging peaks in Fig. 2b and c of the main text (i.e. charging peaks that are adjacent to the gap instead of the additional outside charging peak due to more distant moiré sites). The results are shown in Fig. S10a-c for the n = 1/3, 2/3, and 1 states, respectively. The blue and yellow scatter points correspond to the electron and hole charging peaks, respectively. We next fit the dispersive electron and hole charging peaks with two parallel lines: 1). $V_{BG} = k(V_{bias} - V_e)$ and 2). $V_{BG} = k(V_{bias} - V_h)$. The fitted lines are shown in Fig. S10 as dashed lines. Here we have three independent fitting parameters: k (the slope of the two parallel lines), V_e and V_h (horizontal bias offset for the electron and hole charging branch respectively). ΔV_{bias} is determined as $\Delta V_{bias} = V_h - V_e$. The fitted results are n = 1/3: $\Delta V_{bias} = 0.31V \pm 0.07V$, n = 2/3: $\Delta V_{bias} = 0.28V \pm 0.07V$, and n = 1: $\Delta V_{bias} = 0.66V \pm 0.18V$.
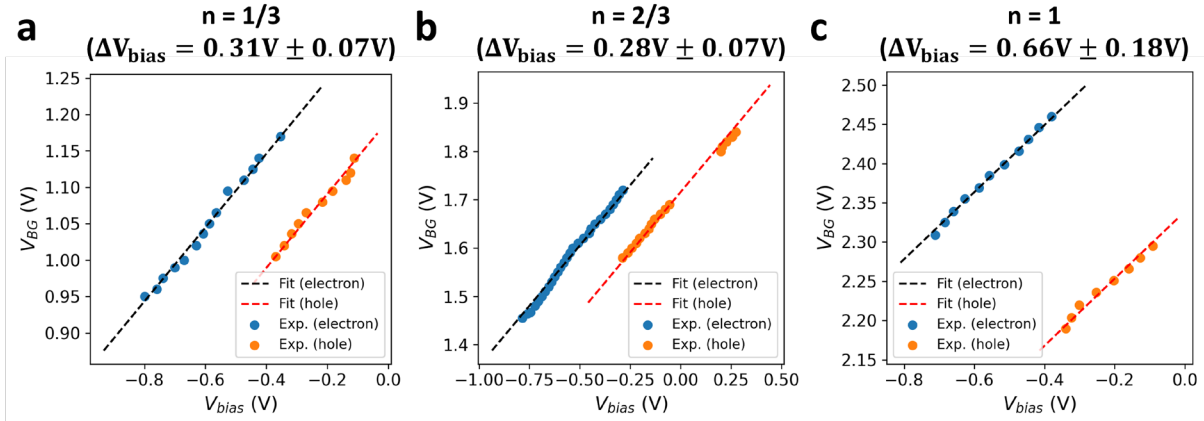
Figure S10. Determination of ΔV_{bias}. Scatter points showing the peak positions of the closest pair of electron and hole charging peaks identified from Fig. 2b,c of the main text (blue: electron charging peak; yellow: hole charging peak). ΔV_{bias} for the n = (**a**) 1/3, (**b**) 2/3, and (**b**) 1 correlated states are determined through fitting the dispersive electron and hole charging peaks with two parallel lines and extracting the horizontal gaps (i.e., ΔV_{bias}) between the fitting lines. The fitting results are n = 1/3: $\Delta V_{bias} = 0.31V \pm 0.07V$, n = 2/3: $\Delta V_{bias} = 0.28V \pm 0.07V$, and n = 1: $\Delta V_{bias} = 0.66V \pm 0.18V$.

8. Spatial distribution of the thermodynamic gaps

Here we demonstrate two examples on how the high spatial resolution of our technique may facilitate the study of moiré correlated electrons.

In Fig. S11 we show the thermodynamic gap distribution in a region with moiré potential disorder. Fig. S11a shows a topographic image of the moiré superlattice (measured in the same region as the one shown in Fig.3d-g of the main text), where no obvious lattice distortion is observed. We next measured the dI/dV spectra at all the $B^{S/S}$ sites labeled with red dots in Fig. S11a with V_{BG} = 1.50V and V_{TG} = 0.52V, that enable us to obtain the thermodynamic gap for n = 2/3 state $\Delta_{n=2/3}$ at different sites. The result is shown in Fig. S11b, where each hexagon corresponds to one $B^{S/S}$ site (red dot) in Fig. R1a. The $\Delta_{n=2/3}$ shows a non-uniform distribution. It is lower at the bottom left corner and higher at the top right corner. This gap distribution is consistent with the nonuniform charging maps shown in Fig.3d-g.

We next show the thermodynamic gaps measured at regions with different moiré superlattice structures. Fig. S12a-c shows topographic images of the moiré superlattices measured in three different regions that exhibit different moiré period L and moiré unit cell distortion δ (see the exact definition below) (hexagons are marked to indicate the lattice distortion). The thermodynamic gaps are measured in the three regions. The lattice structure and the gap values are summarized in Fig. S12d, which shows smaller gaps in moiré superlattices with larger period/distortion.

Unit cell distortion δ in the moiré superlattice was modeled by defining strained moiré primitive lattice vectors: $\boldsymbol{a}_i \to L\boldsymbol{R}(\theta)\boldsymbol{S}(\delta)\boldsymbol{R}(-\theta)\boldsymbol{e}_i$, where $\boldsymbol{R}$ is a 2D rotational matrix, $\boldsymbol{S}(\delta) = \begin{pmatrix} 1+\frac{\delta}{2} & 0 \\ 0 & 1-\frac{\delta}{2} \end{pmatrix}$, $\boldsymbol{e}_i$ is the unit primitive lattice vector, and L is the (undistorted) moiré period.

We believe that the high spatial resolution of our technique could enable more fruitful studies of how moiré structure and disorders impact the moiré correlated electrons, which will be explored in further works.
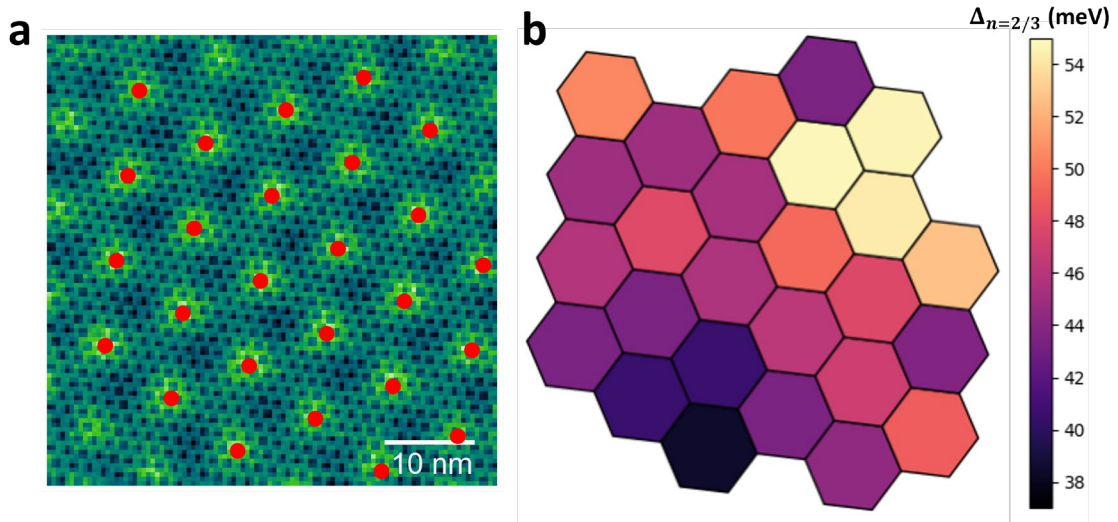

Figure S11. Spatial mapping of $\Delta_{n=2/3}$. a. Topographic image of a typical moiré superlattice region (the same as the one shown in Fig. 3d-g of the main text). dI/dV spectra are measured at all the $B^{S/S}$ sites labeled with red dots that enables us to extract the values of $\Delta_{n=2/3}$. $V_{BG} = 1.50V$ and $V_{TG} = 0.52V$. **d.** Mapping of $\Delta_{n=2/3}$. Each hexagon corresponds to one $B^{S/S}$ site (red) in (**a**) with the filling color represent the value of $\Delta_{n=2/3}$.
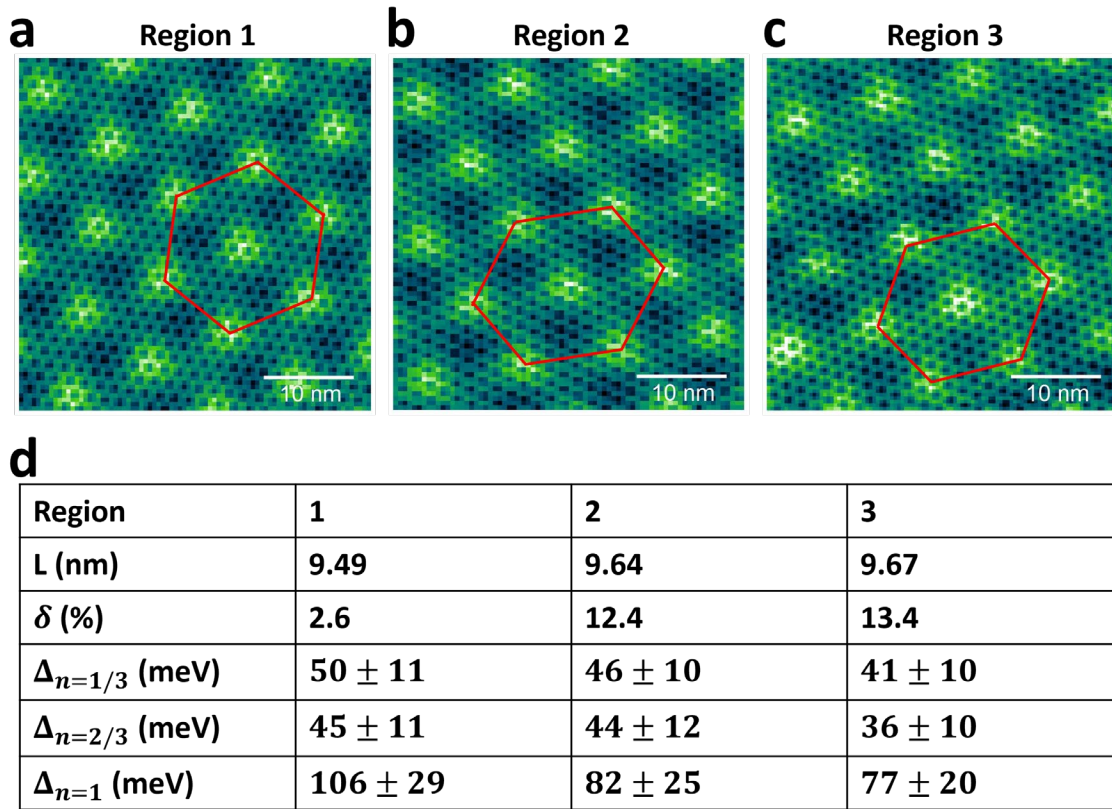
Figure S12. Thermodynamic gaps measured in different moiré superlattice regions. a-c.

Typical topographic images of moiré superlattices measured in three different regions that

exhibit different moiré lattice structure. **d**. Table that summarizes the lattice constant (L), moiré

unit cell distortion (δ), and thermodynamic gaps for the n = 1/3, 2/3, and 1 states ($\Delta_{n=1/3}$,

$\Delta_{n=2/3}$, and $\Delta_{n=1}$).

Reference:

1   Pradhan, N. A., Liu, N., Silien, C. & Ho, W. Atomic scale conductance induced by single impurity charging. *Physical review letters* **94**, 076801 (2005).
2   Brar, V. W. *et al.* Gate-controlled ionization and screening of cobalt adatoms on a graphene surface. *Nature Physics* **7**, 43-47 (2011).
3   Teichmann, K. *et al.* Controlled charge switching on a single donor with a scanning tunneling microscope. *Physical review letters* **101**, 076103 (2008).
4   Wong, D. *et al.* Characterization and manipulation of individual defects in insulating hexagonal boron nitride using scanning tunnelling microscopy. *Nature nanotechnology* **10**, 949-953 (2015).
5   Li, H. *et al.* Imaging local discharge cascades for correlated electrons in WS2/WSe2 moiré superlattices. *Nature Physics*, doi:10.1038/s41567-021-01324-x (2021).
6   Li, H. *et al.* Imaging local discharge cascades for correlated electrons in WS2/WSe2 moir\'e superlattices. *arXiv preprint arXiv:2102.09986* (2021).